APPLIED SCIENCES AND ENGINEERING

Enhanced avionic sensing based on Wigner's cusp anomalies

Rodion Kononchuk[1], Joshua Feinberg[2], Joseph Knee[3], Tsampikos Kottos[1]*

Typical sensors detect small perturbations by measuring their effects on a physical observable, using a linear response principle (LRP). It turns out that once LRP is abandoned, new opportunities emerge. A prominent example is resonant systems operating near *N*th-order exceptional point degeneracies (EPDs) where a small perturbation $\varepsilon \ll 1$ activates an inherent sublinear response $\sim \sqrt[N]{\varepsilon} \gg \varepsilon$ in resonant splitting. Here, we propose an alternative sublinear optomechanical sensing scheme that is rooted in Wigner's cusp anomalies (WCAs), first discussed in the framework of nuclear reactions: a frequency-dependent square-root singularity of the differential scattering cross section around the energy threshold of a newly opened channel, which we use to amplify small perturbations. WCA hypersensitivity can be applied in a variety of sensing applications, besides optomechanical accelerometry discussed in this paper. Our WCA platforms are compact, do not require a judicious arrangement of active elements (unlike EPD platforms), and, if chosen, can be cavity free.

INTRODUCTION

High-sensitivity accelerometers are critical for a variety of technological applications ranging from navigation, gravity gradiometry, structural health, and earthquake monitoring, to platform stabilization for space applications, intruder detection, airbag deployment sensors in automobiles, and consumer electronics protection (*1*–*7*). Their operation relies on the displacement of a test mass that measures acceleration based on a linear response principle (LRP). Developing schemes that go beyond LRP might lead to marked enhancement of small acceleration sensing that, at the same time, does not sacrifice the dynamic range of the sensor. The latter is an important metric in the characteristics of the sensor, and it is defined as the ratio between the maximum and the minimum acceleration that an accelerometer can measure. A prominent example of such sensing protocols is resonant systems operating near *N*th-order exceptional point degeneracies (EPDs) (*8*, *9*), where a small perturbation $\varepsilon \ll 1$ activates an inherent sublinear response $\sim \sqrt[N]{\varepsilon} \gg \varepsilon$ in resonant splitting (*10*–*13*). Its implementation using microresonators (*14*, *15*) led to the realization of a class of EPD-based avionic devices such as EPD gyroscopes (*16*, *17*). The latter is typically formed by judiciously distributing gain between interacting modes of a (photonic) cavity, often leading to excessive quantum noise effects that might inhibit the enhanced sensing (*11*, *17*, *18*). Here, we propose and demonstrate a class of accelerometers with enhanced sensitivity that rely on sublinear variations of scattering cross sections to small perturbations. This response is a consequence of the photonic implementation of Wigner's cusp anomalies (WCAs) occurring at the threshold between an open and closed scattering channel (*19*, *20*).

Let us first outline the fundamental principle associated with WCA (*19*). Although we are using quantum-mechanical language, the description is generic to any linear wave framework. From the principle of detailed balance, one has the following relation between the reaction cross sections $\frac{1}{v_f^2}\frac{d\sigma_{fi}}{d\Omega_f} = \frac{1}{v_i^2}\frac{d\sigma_{i^*f^*}}{d\Omega_i^*}$, where the subindexes i (f) indicate incident (final) states during the scattering process, v_i (v_f) are the corresponding group velocities, and i* (f*) denote the time-reversed states. Just above threshold of the i → f process, $v_f \sim \sqrt{\varepsilon} \to 0$, where $\varepsilon \equiv E - E_t$ with E_t being the threshold energy determined by the properties of the scattering channel and E being the energy of the incident particle. Consider the reverse process f → i at $v_f \to 0$. In this limit, from general principles (*21*), the differential cross section $\frac{d\sigma_{i^*f^*}}{d\Omega_i^*} \sim 1/v_f$. Substituting the latter in the detailed balancing relation, we obtain

$$\frac{d\sigma_{fi}}{d\Omega_f} \sim v_f^2 \cdot \left(\frac{1}{v_f}\right) \sim \sqrt{\varepsilon} \tag{1}$$

which is, loosely speaking, a manifestation of Wigner's cusp (*21*) (see Fig. 1A). The expression Eq. 1 vanishes at $\varepsilon = 0$ since it assumes a single open channel. For the generic case and more details and rigorous derivation, see the Supplementary Materials. In simple terms, the behavior $\frac{d\sigma_{fi}}{d\Omega_f} \sim v_f$ near threshold demonstrates the well-known fact that in scattering processes between propagating modes carrying currents J_i and J_f, the transmittance is $T_{fi} \sim J_f/J_i \sim v_f/v_i$ where $v_i \sim \sqrt{E}$.

Inspired by the sublinear hypersensitivity associated with the resonant detuning near EPDs, we propose to use the sublinear Puiseux expansion for the reflectance/transmittance, near threshold, for hypersensitive sensing. It is important to stress that, as opposed to current sublinear EPD sensing proposals (*14*–*17*), our WCA protocol is based on intensity measurements (i.e., transmittance/reflectance) and does not rely on measuring the resonant shift. The latter is sometimes masked by broadening of the transmission (or the reflection) spectrum or, in case of gain elements, by the unavoidable addition of quantum noise into the system (*11*, *17*, *18*). We therefore propose the WCA as a simple, yet powerful hypersensing platform for a variety of applications ranging from avionics to bio- and chemical sensing.

RESULTS

WCAs in different physical platforms

The simplest example leading to WCA is one-dimensional scattering of a nonrelativistic particle by a step potential of height U extending

[1]Wave Transport in Complex Systems Laboratory, Department of Physics, Wesleyan University, Middletown, CT 06459, USA. [2]Department of Mathematics and Haifa Research Center for Theoretical Physics and Astrophysics, University of Haifa, Mt. Carmel, Haifa 31905, Israel. [3]Department of Chemistry, Wesleyan University, Middletown, CT 06459, USA.
*Corresponding author. Email: tkottos@wesleyan.edu.

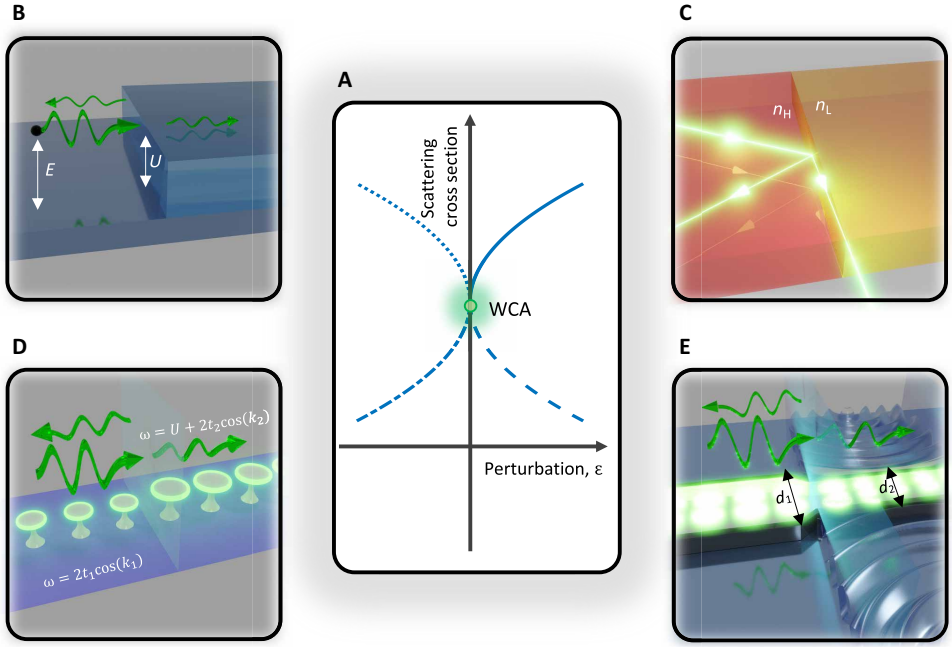

Fig. 1. Various WCA settings. (**A**) A WCA describing a square-root behavior of the scattering cross section in the vicinity of a channel threshold. Various forms of WCA are represented by different line styles (for details, see the Supplementary Materials). (**B**) Scattering of a quantum particle from a step potential of height *U*. (**C**) Near TIR of a monochromatic wave from the interface between two dielectric media with reflection indices $n_i = n_H > n_f = n_L$. (**D**) Two CROW transmission lines with resonant frequency detuning *U*. (**E**) A waveguide whose (right) portion is exposed to pressure variations leading to a distortion of its cross section, which induces a threshold WCA.

over $x \geq 0$ (see Fig. 1B). For $x < 0$, the energy dispersion relation is $E = k_i^2$ (units of $\hbar^2/2m = 1$) where E and k_i are the incident energy and the wave vector, while for $x > 0$, we have $k_f = \sqrt{E-U}$. Threshold occurs at energy $E_t = U$, signifying a transition from a real (for $E > E_t$) to an imaginary (for $E < E_t$) wave vector k_f (corresponding to an evanescent wave). Above (below) threshold $E > U (E < U)$, the reflectance is $R = \left(\frac{k_f - k_i}{k_f + k_i}\right)^2 \approx 1 - 4\sqrt{\frac{E-U}{U}}$ $(R = 1)$, while the corresponding transmittance is $T = 4\frac{k_i k_f}{(k_f + k_i)^2} \approx 4\sqrt{\frac{E-U}{U}}$ $(T = 0)$, which nicely demonstrates the leading square-root term of the systematic Puiseux expansion of these quantities.

The analogous scenario in optics is associated with light scattering through a dielectric interface from a medium with high refractive index $n_i = n_H$ to a medium with a low refractive index $n_f = n_L$ (see Fig. 1C). Assuming that the direction of the normal from the boundary plane is along the z axis, the problem is rotation-invariant around this axis. Consequently, without loss of generality, the direction of propagation can be taken to lie in the xz plane. The dispersion relations on each side of the interface are $k_{i,f}^z = \sqrt{(\frac{\omega}{c} n_{i,f})^2 - (k^x)^2}$, where $\mathbf{k} = (k^x, k^y, k^z)$. Furthermore, $k^x = \frac{\omega}{c} n_i \sin\theta_i$, where θ_i is the incidence angle with respect to the normal to the interface and Snell's law guarantees continuity of k^x. Here, threshold behavior occurs at the critical angle $\theta_i = \theta_c = \arcsin(\frac{n_L}{n_H})$, corresponding to $k_f^z = 0$. The reflection r and transmission t amplitudes are given by the same expressions as in the quantum step example, with k_i and k_f substituted by $k_{i,f}^z$. Just below the critical angle $\theta = \theta_c - \varepsilon$ $(0 < \varepsilon \ll 1)$, we can expand r, t in a Puiseux series, leading to the polarization-dependent reflectance (transmittance)

$$R \equiv |r|^2 \propto 1 - 2A_\delta\sqrt{\varepsilon}, T \equiv |t|^2 \propto 2A_\delta\sqrt{\varepsilon} \qquad (2)$$

where $A_\delta = 2\gamma_\delta^2\sqrt{2(\tilde{n}^2 - 1)}^{-\frac{1}{2}}, \tilde{n} = n_H/n_L$ is a refractive index ratio between the two media, $\delta = p, s$ denotes the s- and p-polarized light, respectively, and $\gamma_{\delta=s} = 1$, while $\gamma_{\delta=p} = \tilde{n}\, n$. These equations show that this scattering process results in the formation of a WCA associated with the opening/closing of a scattering channel k_f^z at a critical incidence angle θ_c.

WCAs are ubiquitous and can be implemented in a variety of other photonic platforms. We can, for example, implement them in one-dimensional coupled resonators optical waveguide (CROW) arrays at the vicinity of a band edge. A simple realization is shown in Fig. 1D, where two CROW arrays with resonant detuning $0 < U < 2|t_1 + t_2|$ and coupling constants $t_{1,2} < 0$ are brought together. When the detuning U varies (e.g., due to exposure of one of the two CROWs to a biological agent or changes of the ambient temperature or illumination), the transmittance/reflectance exhibits WCA for frequencies near the band edges associated with the common transmission frequency domain (see the Supplementary Materials for detailed analysis). Another implementation of WCA involves a uniform multimode waveguide (see Fig. 1E) in the vicinity of a mode threshold. In this case, cross-sectional variations (e.g., due to pressure variations) will induce the closing/opening of a channel at one portion of the waveguide, which, in turn, will be sensed as transmittance changes following a sublinear WCA (see the Supplementary Materials).

Experimental implementation of a WCA avionic sensor

As proof of concept, we have demonstrated the hypersensitive nature of WCA sensors for acceleration measurements. The experimental platform (see Materials and Methods) is shown in Fig. 2 (A and C) and uses the square-root threshold behavior due to total internal reflection (TIR). It involves a Gaussian linear polarized beam,

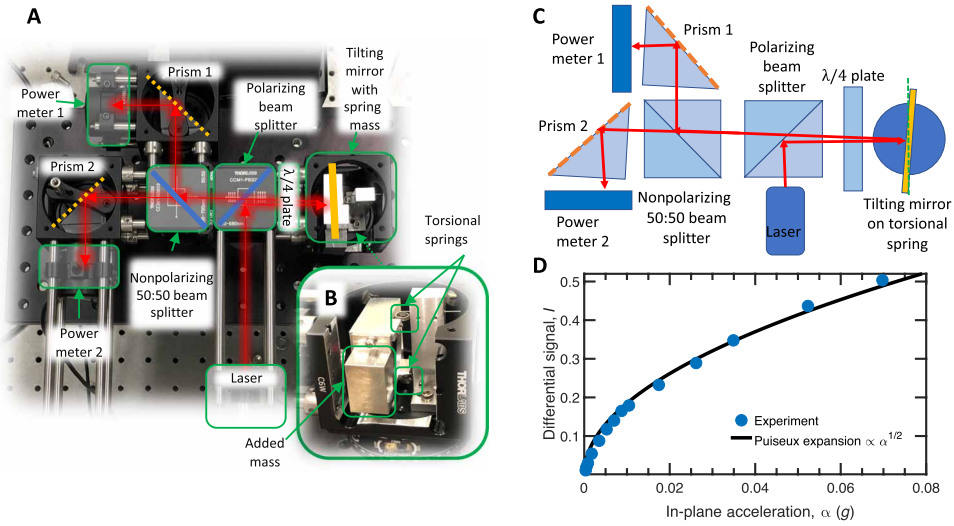

Fig. 2. WCA accelerometer. (**A**) Experimental implementation of the TIR as a WCA protocol for a hypersensitive accelerometer. (**B**) Magnification of the mirror with the attached test mass that is coupled to two torsional springs. (**C**) Schematic description of the platform shown in (A). (**D**) Measured differential signal *I* versus in-plane acceleration α (filled blue circles). The system is calibrated to demonstrate a TIR when it is at rest. Any acceleration will lead to a WCA. The black line indicates the Puiseux expansion near WCA. Photo credit: (A and B) Rodion Kononchuk, Wesleyan University.

produced by a continuous wave (CW) laser source at wavelength $\lambda = 635$ nm, which is completely deflected to the right from a polarizing beam splitter and then passes through a λ/4 plate. After retroreflection from a "tilting mirror" (see Fig. 2, A and B), it goes through the λ/4 plate again, thus resulting in a total of 90° polarization rotation of the beam. Then, the beam goes first through the polarizing beam splitter and subsequently through a 50:50 beam splitter with half of the light propagating straight while the other half is being reflected by 90°. Each of the two beams scatters by a 90° prism (prism 1 and prism 2 in Fig. 2, A and C), which are mounted on high-precision tunable rotational stages. These prisms are positioned in such a way that light is incident on their bottom interface (orange dashed lines in Fig. 2, A and C) at a critical angle whenever the rotating mirror is tilted by an angle $\Delta\theta = 0°$ with respect to a reference plane (green axis in Fig. 2C). Last, the light reflected back from the bottom interface reaches the power meters where it is detected. If the rotating mirror is tilted counterclockwise, the signal on the first power meter I_1 (corresponding to the reflected power) will decrease from its maximum value I_{max} (achieved in the case of TIR) following a square-root behavior (see Eq. 1). Conversely, the light detected by the second sensor I_2 will undergo TIR, yielding maximal measured signal $I_2 = I_{max}$ and vice versa if the mirror is tilted clockwise. To compensate for any low-frequency power instabilities of the laser, it is better to measure the differential signal

$$I = \frac{I_1 - I_2}{I_1 + I_2} = \frac{R_1 - R_2}{R_1 + R_2} \quad (3)$$

where R_1 and R_2 are the reflectances from the bottom interface of prisms 1 and 2, respectively. The differential signal I takes values within the interval $I \in [-1,1]$. Its magnitude indicates the amount that the rotating mirror has been tilted, while its sign indicates the tilt direction of the mirror.

Let us lastly point out that our setup was arranged in such a way that the incident beam at the two prisms 1 and 2 is *p*-polarized. This choice is motivated by the fact that the reflection coefficient A_δ in the vicinity of the critical angle θ_c is enhanced for a *p*-polarized light as compared to the reflection coefficient of an *s*-polarized light (see Eq. 2). As a result, sensitivity to the applied acceleration is also enhanced, allowing us to use smaller mirror tilts for acceleration sensing.

We turn our platform into a highly sensitive accelerometer by attaching the tilting mirror to a spring-mass system (see the inset of Fig. 2B). The latter consists of a pivoting steel mass connected to a pair of torsional springs (see Materials and Methods). This design allows us to sense the in-plane accelerations by monitoring the direction and magnitude of the angular displacement of the mass with the attached mirror. The setup is mounted on a platform that is attached to an electronically controlled rotational stage that monitors the in-plane component of the gravity acceleration α by inclining the stage from the horizontal position. In Fig. 2D, we show the measured differential signal I versus the applied in-plane acceleration α (filled blue circles). The data agree with the Puiseux expansion $I \propto \sqrt{\alpha}$ (black line), which is applicable in the vicinity of WCA, thus establishing our sensing scheme as a hypersensitive accelerometer.

In Fig. 3A, we report the experimental data for the differential signal I versus the in-plane acceleration α in a log-log plot. We observe that for very small accelerations, $\alpha \leq \alpha_{GHS} \approx 10^{-3}\,g$, the differential signal deviates from the square-root behavior (black dotted line) and becomes a linear function of the acceleration, i.e., $I \sim \alpha$ (black dashed line). These deviations are attributed to the Gaussian shape of our beam and the associated beam divergence. The latter leads to Fresnel filtering and to an angular Goos-Hänchen shift (GHS) (*22*–*24*), which is the source of departure from the sublinear square-root behavior (see the Supplementary Materials). To substantiate this statement, we have performed calculations that take into consideration the beam divergence ($\vartheta_{GHS} = 0.3$ mrad) of the laser used in our experiments (red solid line). We have found that α_{GHS} is determined by a mirror tilt that is comparable with the laser beam half-divergence $\vartheta_{GHS} = \frac{\lambda}{\pi n w_0}$ (see Materials and Methods and the Supplementary Materials). Obviously, a laser beam with a shorter

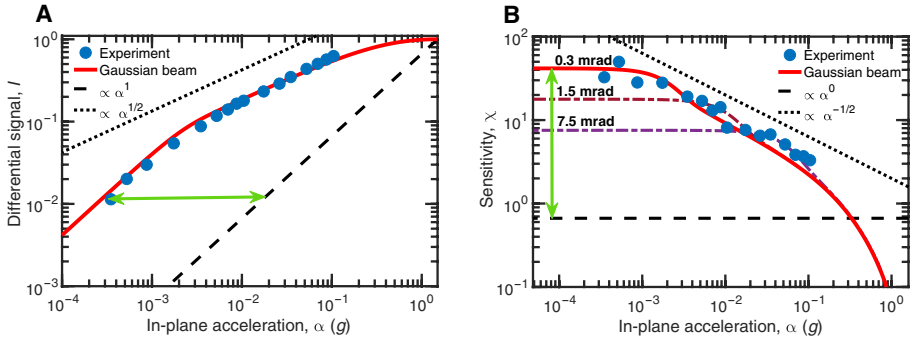

Fig. 3. Beam divergence effects and WCA-sensitivity. (**A**) Measured differential signal *I* versus in-plane accelerations α (blue filled circles) reported in log-log plot. The theoretical calculation that incorporates the Gaussian beam divergence of 0.3 mrad is shown in the red solid line. The black dotted line has a slope of $^1/_2$, while the black dashed line indicates the linear slope of the conventional acceleration sensor with the same maximum output and with linear sensitivity. The green double-sided arrow indicates the dynamic range enhancement of the proposed WCA sensor. (**B**) Measured sensitivity of the accelerometer $\chi \equiv dI/d\alpha$ (blue filled circles). The red solid line describes the theoretical curve that takes into consideration the Gaussian beam divergence associated with the characteristics of our lasing source (0.3-mrad beam divergence). In the same figure, we also report with a dark red (purple) dashed-dotted line the theoretically calculated sensitivity for a lasing source with a beam divergence of 1.5 mrad (7.5 mrad). The black dotted line has a slope of $-^1/_2$, while the black dashed line indicates a constant sensitivity $\chi = 0.67\ g^{-1}$ of a conventional linear accelerometer (see the main text). The green double-sided arrow indicates the sensitivity enhancement of the proposed WCA sensor.

wavelength and/or a larger waist w_0 will further reduce the GHS bound and enhance the sublinear range. Nevertheless, even in the GHS linear range, the response of our WCA platform is superior to typical linear accelerometers as discussed below.

To quantify its efficiency, we have introduced the sensitivity (*25*) $\chi \equiv dI/d\alpha$. In Fig. 3B, we report the experimentally measured sensitivity together with the corresponding theoretical results, which incorporate the beam divergence of our laser source (red line). We have found that the WCA sensitivity χ increases as we move toward smaller accelerations, reaching a constant value that is approximately $41.6g^{-1}$ in the GHS regime. To demonstrate the effect of beam divergence on sensitivity, we are also reporting at the same Fig. 3B the theoretical predictions for two other χ's, corresponding to larger beam divergences (see the dark red and purple dashed-dotted lines).

At the same time, our analysis indicates that at large accelerations ($\alpha \approx \alpha_{max} = 1.5\ g$), the differential signal approaches a saturation value $I_{max} = 1$ (see Fig. 3A). This upper bound is associated with a tilt of the test-mass mirror that leads to zero reflection of the *p*-polarized light from either of the two sensing prisms 1 or 2. The latter occurs whenever the angle of the incident beam at the bottom interfaces of these prisms is equal to the Brewster angle θ_b.

In contrast, a conventional linear accelerometer with the same upper bound of dynamic range ($\alpha_{max} = 1.5\ g$ corresponding to $I_{max} = 1$) has constant sensitivity $\chi = I_{max}/\alpha_{max} = 0.67\ g^{-1}$ for any applied acceleration (see black dashed line in Fig. 3B). We deduce, therefore, that even in the GHS regime, our proposed WCA protocol demonstrates a 60-fold improved performance as compared to conventional linear accelerometers (see the green arrow in Fig. 3B). The latter is translated to a similar enhancement of the lower bound of the dynamic range α_{min} (see the green arrow in Fig. 3A).

Noise analysis

To further characterize the performance of the WCA accelerometer, we have analyzed the various sources of noise that might affect its sensitivity. The fundamental limit of sensitivity for all test-mass accelerometers is given by the thermal motion of the mass, which is known as the thermal noise equivalent acceleration $\alpha_{th} = \sqrt{\frac{4k_bT\omega_n}{mQ}}$ (*26*, *27*). In this expression, k_b is the Boltzmann's constant, $T = 293.15$ K is the ambient temperature, $m = 0.027$ kg is the mass, ω_n is the natural angular frequency, and *Q* is the quality factor of the resonant mode of the mechanical test mass. Notice that α_{th} can be further reduced by maximizing the mass-*Q* product at a given ω_n [see (*3*)]. We extracted these parameters for our system by analyzing the power spectral density (PSD) *S*(*f*) of the time-dependent differential signal *I*. These measurements were performed over a long period of time with the sensor at rest and with data being recorded with a sampling frequency of 16.6 Hz. The measured frequency response is shown in Fig. 4A (blue line) and demonstrates a resonant peak at $\omega_n \approx 2\pi \times 3.95$ Hz. From a Lorentzian fit (green line), we extracted the mechanical *Q* factor ≈28. Knowledge of these parameters allows us to estimate $\alpha_{th} \approx 7.4 \times 10^{-11}\ g{\cdot}\mathrm{Hz}^{-\frac{1}{2}}$ [corresponding to lower bound of the measured acceleration $\langle\alpha\rangle = \alpha_{th} \cdot \sqrt{\Delta f} \approx 10^{-10}\ g$ where $\Delta f \approx \omega_n/2\pi$] (*28*). There are also other types of noise sources related to, e.g., displacement read-out noise (α_{det}) or added noises (α_{add}) associated with the laser source and electronics used in the measurements. Although α_{det} and α_{add} can be actively minimized, their presence usually prohibits the total noise equivalent acceleration $\alpha_{nea} \equiv \sqrt{\alpha_{th}^2 + \alpha_{det}^2 + \alpha_{add}^2}$ from reaching its minimal value α_{th}.

To obtain cumulative quantification of noise effects on the measured signal *I*, we have evaluated the Allan deviation (*29*) σ_I (see Eq. 10 in Materials and Methods) for two cases corresponding to $\alpha = 0\ g$ (blue line) and $\alpha = 0.026\ g$ (dotted magenta line) (see Fig. 4B). The corresponding colored highlights indicate 1 SD $\sigma_I \pm \delta\sigma_I$. Allan deviation describes the stability of the system as a function of the sampling time τ. From our analysis, we find that both cases result in (essentially) identical σ_I, indicating that the noise in the measured signal *I* is not enhanced by the proximity of the system to the WCA.

In Fig. 4C, we report the normalized Allan deviation $\sigma_\alpha = \sigma_I/\chi$, thus providing an estimate of the total noise effect on the measured acceleration. In particular, the short-time decay of the Allan deviation [velocity random walk (VRW)] behaves like $\sigma_{VRW}(\tau) = \alpha_{nea} \cdot \tau^{-1/2}$, with best fit $\alpha_{nea} = 0.65 \times 10^{-5}\ g{\cdot}\mathrm{Hz}^{-\frac{1}{2}}$ for $\alpha = 0\ g$ (red dotted line in Fig. 4C) and $\alpha_{nea} = 5.46 \times 10^{-5}\ g{\cdot}\mathrm{Hz}^{-\frac{1}{2}}$ for $\alpha = 0.026\ g$ (red dashed line in Fig. 4C). In addition, the large-time growing part of σ(τ) allows us to extract the so-called acceleration random walk

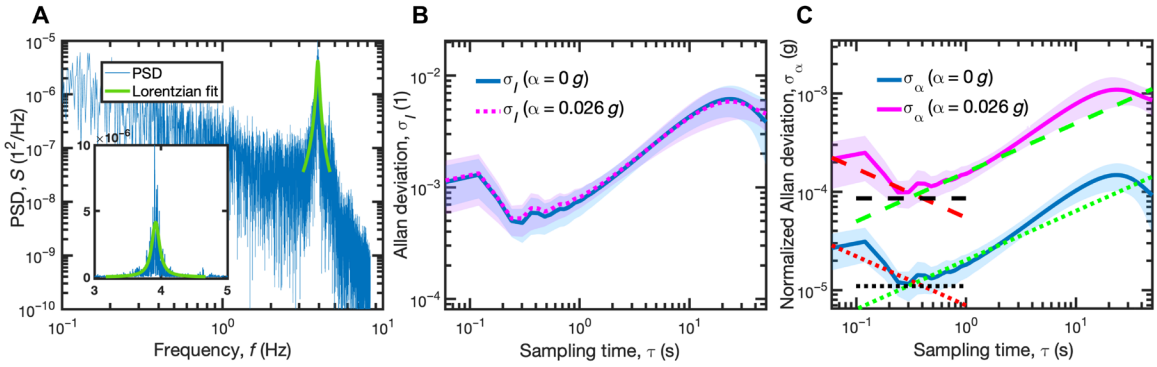

Fig. 4. Noise analysis. (**A**) The PSD of the output signal *I* versus the sampling frequency when the sensor is at rest (blue solid line). The green line is a Lorentzian fit of the mechanical resonant mode (inset: the same data reported in linear scale). (**B**) Averaged (over four measurements) Allan deviation σ_I versus sampling time τ for the WCA accelerometer for $\alpha = 0\ g$ (blue line) and $\alpha = 0.026\ g$ (dotted magenta line). (**C**) The normalized Allan deviation σ_α in acceleration units versus the sampling time τ when the accelerometer is in the proximity of a WCA ($\alpha = 0\ g$, blue line) and away from a WCA ($\alpha = 0.026\ g$, magenta line). The BI (σ_{BI}) fit is shown by the black dotted (dashed) line, the VRW (σ_{VRW}) is shown by the red dotted (dashed) line, and the ARW (σ_{ARW}) is shown by the green dotted (dashed) line. The highlighted domains around the lines of the same color in (B) and (C) denote the distance from the averaged σ_I by (±) 1 SD.

(ARW), which describes exponentially correlated noise with a very long correlation time. By definition, $\sigma_{ARW}(\tau) = \alpha_{ARW} \cdot \sqrt{(\tau/3)}$, with best fit $\alpha_{ARW} = 3.5 \times 10^{-5}\ g{\cdot}s^{-1} \cdot Hz^{-\frac{1}{2}}$ for $\alpha = 0\ g$ (green dotted line) and $\alpha_{ARW} = 2.2 \times 10^{-4}\ g{\cdot}s^{-1} \cdot Hz^{-\frac{1}{2}}$ for $\alpha = 0.026\ g$ (green dashed line). Last, the saturation value $\sigma_{BI}(\tau) = \alpha_{BI} \cdot \tau^0$ of the Allan deviation (black dashed line) is indicative of the bias instability (BI) and sets the smallest possible reading of our sensor because of the random flickering of electronics or other components. The extracted value is $\alpha_{BI} = 1.1 \times 10^{-5}\ g$ for $\alpha = 0\ g$ (black dotted line) and $\alpha_{BI} = 8.58 \times 10^{-5}\ g$ for $\alpha = 0.026\ g$ (black dashed line). From this analysis, we conclude that the effect of noise in the measured acceleration is reduced in the vicinity of the WCA where the sensitivity of our platform acquires its maximum value. This result has to be contrasted with an enhanced noise level near an EPD, which originates from the use of gain elements and which offsets the enhanced signal sensitivity (*17*, *18*). We also mention that the dynamic range of our accelerometer can be estimated by the ratio of α_{max} to α_{BI} (corresponding to $\alpha = 0\ g$), and it is approximately equal to 50 dB. Such dynamic range is comparable to state-of-the-art nanofabricated optomechanical accelerometers (*3*, *4*).

Let us lastly point out that the thermal noise $\alpha_{th} = 7.4 \times 10^{-11}\ g{\cdot}Hz^{-\frac{1}{2}}$ is independent of the proximity of our platform to the WCA and depends only on the parameters that affect the mechanical degree of freedom (spring mass). As a result, α_{th} sets the fundamental limit of the acceleration resolution for short sampling times. A comparison with the value $\alpha_{nea} = 0.65 \times 10^{-5}\ g{\cdot}Hz^{-\frac{1}{2}}$, assocciated with the noise equivalent acceleration at $\alpha = 0\ g$, indicates that α_{th} is five orders of magnitude smaller than α_{nea}, and therefore, it has negligible effect on Allan deviation at the vicinity of the WCA. Consequently, the normalized Allan deviation $\sigma_\alpha = \sigma_I/\chi$ shown in Fig. 4C is reduced by one order of magnitude (when comparing the cases for $\alpha = 0\ g$ and $\alpha = 0.026\ g$) because of the corresponding enhanced sensitivity χ (by one order) demonstrated by our platform at the vicinity of WCA.

DISCUSSION

We have proposed a class of sensors with enhanced sensitivity due to sublinear (Puiseux) expansion of the transmittance/reflectance near a threshold frequency of an open-to-close channel. At such frequencies, the scattering matrix elements develop a square-root behavior, i.e., WCA with respect to small perturbations, in contrast to the linear response used in standard arrangements. As an example, we have demonstrated the efficiency of our protocol by designing a hypersensitive WCA accelerometer.

The proposed protocol is likely to have advantages compared to other sensor schemes whose operational principle relies on abrupt intensity variations. A typical example is offered by fiber Bragg grating (FBG) sensors (*30*, *31*) that detect the variations in the transmission $T(\lambda)$ due to spectral shifts induced by small perturbations ε that modify the effective index of the fiber modes. The largest possible change in the transmitted power (which is used to infer the strength of the applied perturbation) occurs when probe light is injected at a wavelength λ_{probe} tuned to the steepest portion of the transmission spectrum. Ideal candidates are slow light resonances with high Q factor (large group delay τ_g). They occur either at π-shifted gratings or at the edges of a bandgap in a strong FBG. Their implementation leads to FBG sensors with sensitivity $\chi = (dT/d\varepsilon)\,|_{\lambda probe} = (dT/d\lambda)\,|_{\lambda probe} d\lambda_B/d\varepsilon$, where λ_B is the Bragg wavelength and $(dT/d\lambda)\,|_{\lambda probe} \sim \tau_g$. Apart from the fact that these schemes rely on high-Q resonances (compared with our proposal that does not require any cavity), they also suffer from a trade-off between minimum and maximum detectable measurands. As the slope of the resonance increases (higher sensitivity), the maximum detectable measurand decreases in an inversely proportional manner, thus leading to a reduced dynamic range—the other important metric that characterizes the efficiency of a sensor.

WCA sensors might also be advantageous compared to recent Puiseux-based sensors that use EPDs. The latter, depending on the optical platform used to implementing them, might suffer from quantum-noise effects related to the strong mode nonorthogonality in the proximity of an EPD. Specifically, recent experiments with EPD-based Brillouin ring laser gyroscopes indicated that the enhanced sensitivity is exactly counterbalanced by an excess quantum noise whose origin has been traced to the increase of the Petermann factor in the proximity of the EPD (*17*, *18*). These EPD-based sensors require a judicious arrangement of gain and

loss elements as opposed to our proposal that is easy to manufacture and can be cavity free. Last, we point out that the proposed WCA sensor is based on intensity measurements, thus avoiding undesirable resolution limitations due to potential resonance broadening.

MATERIALS AND METHODS

Experimental setup

A photograph of the experimental optical setup is shown in Fig. 2A. It is assembled using Thorlabs 30-mm cage components. The source is a CW 635-nm, 1.2-mW, round beam diode laser CPS635R with 0.017° (0.3 mrad) half-beam divergence. The polarizing beam splitter is a 30-mm cage cube CCM1-PBS251, while the nonpolarizing 50:50 beam splitter is a 30-mm cage cube CCM1-BS013. The quarter–wave plate used in the setup is WPQ10ME-635. The setup also incorporates two ultraviolet (UV)–fused silica 25-mm 90° prisms (see prism 1 and prism 2 in Fig. 2, A and C), mounted on a mechanically controlled high-precision 30-mm cage rotational stage B4CRP. The beam passing through the prism was focused using a 1-inch-diameter lens with a focal distance of 25.4 mm on the photodiode power meter PM16-120 with a 9.5-mm aperture, which allows the beam to reach the sensor area when it is deflected owing to the mirror tilt.

For the acceleration sensing measurements (see Figs. 2D and 3A), a backside polished broadband dielectric mirror BB1-E02P was mounted inside an aluminum frame with an added steel mass of 0.027 kg on one side that is pivoting on a pair of torsional right- and left-handed springs TMR/L-0160-017 and is mounted inside the 30-mm cage cube on a mechanically controlled rotational stage B4CRP (see Fig. 2B). This mechanical piece was designed using the structural mechanical module of the COMSOL multiphysics software. It acts as a spring mass tilting the mirror in clockwise/counterclockwise direction depending on the direction of the applied in-plane acceleration. The whole sensing platform was mounted on the optical breadboard attached to the rotational stage Newport URS100BCC with 2 mdeg (0.035 mrad) minimal angular increment, electronically controlled with a Newport ESP301 controller. The setup allows us to control the horizontal tilt of the platform and, thus, the in-plane component of the gravity acceleration. Before taking the measurements, the setup was precisely tuned by aligning the system to the close vicinity of the critical angle of propagation through both prisms simultaneously. This was done by monitoring the power on each power meter independently while rotating the relevant 90° prism and matching the received power with the numerical calculations of the Gaussian beam propagation through the fused silica/air interface. The signal on the power meters was calibrating to account for uneven beam splitting provided by the beam splitter CCM1-BS013, which was found to be 47:53. The measured signal at each power meter was sampled with 10^{-5} mW resolution with its maximum value in the TIR regime being as high as 0.538 mW. The corresponding resolution of the differential signal is as low as $I_{\min} = \frac{0.53801 - 0.538}{0.53801 + 0.538} \approx 10^{-5}$, which is 1.5 orders of magnitude smaller than the minimal value of the unnormalized Allan deviation σ_I reported in Fig. 4B. The same difference of 1.5 orders of magnitude applies also between the acceleration resolution $\alpha_{\min} = \frac{I_{\min}}{\chi_5} = 2.2 \times 10^{-7}\, g$ and the measured bias instability $\alpha_{BI} = 8.58 \times 10^{-5}\, g$ (for $\alpha = 0\, g$) reported in Fig. 4C. We conclude, therefore, that the resolution with which the differential signal is measured is sufficient for the results reported in the noise analysis.

Fundamental limits associated with beam divergence

Real optical beams with finite width have distributed plane wave spectra and are subjected to several lateral and angular shifts (*24*). It is, therefore, important to study the ramifications of these effects in the reflection r and transmission t amplitudes in the vicinity of the critical angle θ_c. For instance, at the vicinity of the critical angle θ_c, the reflection and the transmission of a Gaussian beam (the typical beam shape produced by a laser) experience deviations from Fresnel's laws due to Fresnel filtering (*22*) and the associated angular GHS (*23*). This effect can be understood as follows: When the Gaussian beam (or any other beam with finite width) propagates toward the dielectric interface at the critical angle, it contains angular components that have incident angles larger/smaller than the critical one. The former/latter beam components are totally/partially reflected (Fresnel filtering), forming a combination of propagating and reflected beams with central wave vectors that have an angular shift with respect to the ones predicted by Fresnel's theory (angular GHS on transmission/reflection). Consequently, the reflection r and transmission t amplitudes of a diverging incident beam deviate from the predictions of Fresnel's equations. The reflection components of the divergent beam with a central wave vector $\mathbf{k_0}$ develop small in-plane and out-of-plane components k_μ, $k_\nu \ll 1$. In the *s*- and *p*-polarization basis, these components are related to their corresponding incident components via the following Jones matrix (*24*)

$$\begin{pmatrix} E_p^{\mathrm{r}}(\theta) \\ E_s^{\mathrm{r}}(\theta) \end{pmatrix} = \begin{pmatrix} r_p(\theta+\mu) & \nu\, r_p(\theta)\left(1+\frac{r_s(\theta)}{r_p(\theta)}\right)\cot(\theta) \\ \nu\, r_s(\theta)\left(1+\frac{r_p(\theta)}{r_s(\theta)}\right)\cot(\theta) & r_s(\theta+\mu) \end{pmatrix} \begin{pmatrix} E_p^{\mathrm{in}} \\ E_s^{\mathrm{in}} \end{pmatrix} \quad (4)$$

where θ is the angle of incidence of the central wave vector $\mathbf{k_0}$, and we have parametrized the in-plane and out-of-plane components as $k_\mu = \mu k_0$ and $k_\nu = \nu k_0$ with $\mu, \nu \ll 1$. Furthermore, in Eq. 4, r_p and r_s are the reflection amplitudes for the *p*- and *s*-polarization, while $E_{p,s}^{\mathrm{in,r}}$ are the electric field amplitudes associated with the *p*-, *s*-polarization of an incident (in) and reflected (r) wave.

Next, we consider the case of an incident normalized *p*-polarized Gaussian beam with a waist w_0. Such a beam is described as

$$E^{\mathrm{in}} = \begin{pmatrix} E_p^{\mathrm{in}} \\ 0 \end{pmatrix} \quad (5)$$

where $E_p^{\mathrm{in}} = \left(\frac{w_0^2}{2\pi}\right) \cdot e^{-\frac{(k_0 w_0)^2(\mu^2+\nu^2)}{2}}$. The reflected in-plane and out-of-plane beam components are written as

$$E^{\mathrm{r}}(\theta;\mu,\nu) = \begin{pmatrix} E_p^{\mathrm{r}}(\theta;\mu,\nu) \\ E_s^{\mathrm{r}}(\theta;\mu,\nu) \end{pmatrix} = E_p^{\mathrm{in}} \cdot \begin{pmatrix} r_p(\theta+\mu) \\ \nu\, r_s(\theta)\left(1+\frac{r_p(\theta)}{r_s(\theta)}\right)\cot(\theta) \end{pmatrix} \quad (6)$$

The total *p*-polarized and *s*-polarized electric field components of the reflected beam can be found by substituting Eq. 6 on the right-hand-side of Eq. 4. We thus obtain

$$\begin{aligned} E_p^{\mathrm{r}} &= \int E_p^{\mathrm{in}} \cdot r_p(\theta+\mu)\, d k_\mu\, d k_\nu \\ E_s^{\mathrm{r}} &= \int E_p^{\mathrm{in}} \nu \cdot r_s(\theta)\left(1+\frac{r_p(\theta)}{r_s(\theta)}\right)\cot(\theta)\, d k_\mu\, d k_\nu \end{aligned} \quad (7)$$

where integration is carried over the entire k_μ and k_ν real axes.

From Eq. 7, we find that $E_s^r = 0$ since the (symmetric ν-)integration is over an odd function of ν. Therefore, the linear polarization of the beam is preserved during the reflection from the interface. At the same time, we have that at the vicinity of the critical angle θ_c of incidence $E_p^r(\theta_c - \varepsilon - \mu) \approx 1 - A_p\sqrt{\varepsilon + \mu}$, where $A_p = 2\bar{n}^2\sqrt{2(\bar{n}^2 - 1)^{-\frac{1}{2}}}$ (see Eq. 2). Inserting this relation in Eq. 7, we derive the following expression for the *p*-polarized component of the reflected beam

$$E_p^r = \int E_p^{in} \cdot (1 - A_p\sqrt{\varepsilon + \mu})\, d k_\mu \cdot d k_\nu \tag{8}$$

In case of very small deviations of angle of incidence from the critical angle ($\varepsilon \ll \mu$), we can further expand the square root appearing in the parenthesis of Eq. 8 as $\sqrt{\varepsilon + \mu} \approx \sqrt{\mu} + \frac{\varepsilon}{2\sqrt{\mu}}$. Substituting the latter expression in Eq. 8 together with the Gaussian form of the incident wave Eq. 6, we arrive at the expression for the reflection coefficient for the incident *p*-polarized wave. The same analysis can be done for the *s*-polarized light yielding the equations

$$\mathcal{R}e(r_\delta) = 1 - A_\delta \cdot \frac{\Gamma\left(\frac{3}{4}\right)}{2^{3/4}\sqrt{\pi k_0 w_0}} - A_\delta \cdot \frac{\Gamma\left(\frac{1}{4}\right)}{2^{9/4}\sqrt{\pi}}\sqrt{k_0 w_0} \cdot \varepsilon$$

$$\mathcal{I}m(r_\delta) = A_\delta \cdot \frac{\Gamma\left(\frac{3}{4}\right)}{2^{3/4}\sqrt{\pi k_0 w_0}} + A_\delta \cdot \frac{\Gamma\left(\frac{1}{4}\right)}{2^{9/4}\sqrt{\pi}}\sqrt{k_0 w_0} \cdot \varepsilon \tag{9}$$

where we have used the fact that the incident Gaussian beam is normalized and $\delta = s, p$ indicates the polarization of the incident beam. In Eq. 9, $k_0 = \frac{2\pi n}{\lambda}$ with λ being a wavelength, and w_0 is a Gaussian beam waist. Equation 9 holds whenever the deviation from the critical angle $|\varepsilon|$ is smaller than or equal to half of the Gaussian beam divergence: $|\varepsilon| \leq \vartheta_{GHS} = \frac{\lambda}{\pi n w_0}$. Therefore, the beam divergence establishes a bound on how close one can approach the Fresnel limit on the basis of parameters of an incident Gaussian beam. A numerical evaluation of the reflection amplitudes $\mathcal{R}e(r_p)$ and $\mathcal{I}m(r_p)$ of a *p*-polarized Gaussian beam and their comparison with the Fresnel predictions and the associated linear approximation in Eq. 9 is reported in fig. S1.

Allan deviation

The Allan deviation $\sigma_I(\tau)$ is extracted from the long-term measurement of the differential signal *I* with the sensor at rest. It is evaluated from the PSD $S(f)$ as (*29*, *32*)

$$\sigma_I(\tau) = 2\left(\int_0^\infty S(f)\frac{\sin^4(\pi f\tau)}{(\pi f\tau)^2}df\right)^{1/2}. \tag{10}$$

SUPPLEMENTARY MATERIALS

Supplementary material for this article is available at http://advances.sciencemag.org/cgi/content/full/7/23/eabg8118/DC1

REFERENCES AND NOTES

1. P. S. de Brito Andre, V. Humberto, *Accelerometers: Principles, Structure and Applications* (Nova Science Publishers, 2013).
2. M. Bao, *Micro Mechanical Transducers: Pressure Sensors, Accelerometers and Gyroscopes* (Elsevier, 2000).
3. A. G. Krause, M. Winger, T. D. Blasius, Q. Lin, O. Painter, A high-resolution microchip optomechanical accelerometer. *Nat. Photonics* **6**, 768–772 (2012).
4. Y. L. Li, P. F. Barker, Characterization and testing of a micro-g whispering gallery mode optomechanical accelerometer. *J. Light. Technol.* **36**, 3919–3926 (2018).
5. A. Schliesser, O. Arcizet, G. Rivière, G. Anetsberger, T. J. Keppenberg, Resolved-sideband cooling and position measurement of a micromechanical oscillator close to the Heisenberg uncertainty limit. *Nat. Physics* **5**, 509–514 (2009).
6. C. A. Regal, J. D. Teufel, K. W. Lehnert, Measuring nanomechanical motion with a microwave cavity interferometer. *Nat. Physics* **4**, 555–560 (2008).
7. M. A. Taylor, J. Janousek, V. Daria, J. Knittel, B. Hage, H.-A. Bachor, W. P. Bowen, Biological measurement beyond the quantum limit. *Nat. Photonics* **7**, 229–233 (2013).
8. T. Kato, *Perturbation Theory for Linear Operators* (Springer, 2013).
9. M. V. Berry, Physics of non-Hermitian degeneracies. *Czechoslovak J. Phys.* **54**, 1039–1047 (2004).
10. J. Wiersig, Enhancing the sensitivity of frequency and energy splitting detection by using exceptional points: Application to microcavity sensors for single-particle detection. *Phys. Rev. Lett.* **112**, 203901 (2014).
11. J. Wiersig, Prospects and fundamental limits in exceptional point-based sensing. *Nat. Comm.* **11**, 2454 (2020).
12. L. Feng, R. El-Ganainy, L. Ge, Non-Hermitian photonics based on parity-time symmetry. *Nat. Photonics* **11**, 752–762 (2017).
13. M. Parto, Y. G. N. Liu, B. Bahari, M. Khajavikhan, D. N. Christodoulides, Non-Hermitian and topological photonics: Optics at an exceptional point. *Nanophotonics* **10**, 403 (2021).
14. H. Hodaei, A. U. Hassan, S. Wittek, H. Garcia-Gracia, R. El-Ganainy, D. N. Christodoulides, M. Khajavikhan, Enhanced sensitivity at higher-order exceptional points. *Nature* **548**, 187–191 (2017).
15. W. Chen, S. K. Ozdemir, G. Zhao, J. Wiersig, L. Yang, Exceptional points enhance sensing in an optical microcavity. *Nature* **548**, 192–196 (2017).
16. M. P. Hokmabadi, A. Schumer, D. N. Christodoulides, M. Khajavikhan, Non-Hermitian ring laser gyroscopes with enhanced Sagnac sensitivity. *Nature* **576**, 70–74 (2019).
17. Y.-H. Lai, Y.-K. Lu, M.-G. Suh, Z. Yuan, K. Vahala, Observation of the exceptional-point-enhanced Sagnac effect. *Nature* **576**, 65–69 (2019).
18. H. Wang, Y.-H. Lai, Z. Yuan, M.-G. Suh, K. Vahala, Petermann-factor sensitivity limit near an exceptional point in a Brillouin ring laser gyroscope. *Nat. Comm.* **11**, 1610 (2020).
19. E. P. Wigner, On the behavior of cross sections near thresholds. *Phys. Rev.* **73**, 1002–1009 (1948).
20. C. Mahaux, H. A. Weidenmüller, *Shell-Model Approach to Nuclear Reactions* (North-Holland Publishing, 1969).
21. L. D. Landau, E. M. Lifshitz, *Quantum Mechanics* (Pergamon Press, ed. 3, 1977).
22. H. E. Tureci, A. D. Stone, Deviation from Snell's law for beams transmitted near the critical angle: Application to microcavity lasers. *Opt. Lett.* **27**, 7–9 (2002).
23. J. B. Götte, S. Shinohara, M. Hentschel, Are Fresnel filtering and the angular Goos-Hänchen shift the same? *J. Optics* **15**, 014009 (2013).
24. K. Y. Bliokh, A. Aiello, Goos-Hänchen and Imbert-Fedorov beam shifts: An overview. *J. Opt.* **15**, 014001 (2013).
25. X. Jiang, A. J. Qavi, S. H. Huang, L. Yang, Whispering-gallery sensors. *Matter* **3**, 371–392 (2020).
26. K. Y. Yasumura, T. D. Stowe, E. M. Chow, T. Pfafman, T. W. Kenny, B. C. Stipe, D. Rugar, Quality factors in micron- and submicron-thick cantilevers. *J. Microelectromech. Syst.* **9**, 117–125 (2000).
27. A. N. Cleland, M. L. Roukes, Noise processes in nanomechanical resonators. *J. Appl. Phys.* **92**, 2758–2769 (2002).
28. R. Kononchuk, T. Kottos, Orientation-sensed optomechanical accelerometers based on exceptional points. *Phys. Rev. Research* **2**, 023252 (2020).
29. N. El-Sheimy, H. Hou, X. Niu, Analysis and modeling of inertial sensors using Allan variance. *IEEE Trans. Instrument. Measurement* **57**, 140–149 (2008).
30. H. Wen, G. Skolianos, S. Fan, M. Bernier, R. Vallée, M. J. Digonnet, Slow-light fiber Bragg grating strain sensor with a 280-femtostrain/ √ Hz resolution. *J. Light. Technol.* **31**, 1804–1808 (2013).
31. G. Skolianos, A. Arora, M. Bernier, M. Digonnet, Slow light in fiber Bragg gratings and its applications. *J. Phys. D Appl. Phys.* **49**, 463001 (2016).
32. A. G. Quinchia, G. Falco, E. Falletti, F. Dovis, C. Ferrer, A comparison between different error modeling of MEMS applied to GPS/INS-integrated systems. *Sensors* **13**, 9549–9588 (2013).
33. J. Sucher, G. A. Snow, T. B. Day, Cusp phenomena in the region of two neighboring thresholds. *Phys. Rev.* **122**, 1645–1648 (1961).
34. Y. V. Fyodorov, H.-J. Sommers, Statistics of resonance poles, phase shifts and time delays in quantum chaotic scattering: Random matrix approach for systems with broken time-reversal invariance. *J. Math Phys.* **38**, 1918–1981 (1997).
35. T. Kottos, H. Schanz, Statistical properties of resonance widths for open quantum graphs. *Waves Random Media* **14**, S91–S105 (2004).

Acknowledgments

Funding: We acknowledge partial funding from Air Force Office of Scientific Research via grant no. FA 9550-14-1-0037, from NSF-EFMA via grant no. 1641109, and from Simons Collaborations in MPS via grant no. 733698. **Author contributions:** R.K. designed and performed the experiments with the help of J.K. The analysis of the experimental data and the

calculations for the WCA in CROW systems have been performed by R.K. J.F. theoretically derived the WCA for the multimoded scattering case. T.K. conceived and supervised the project and assisted with the theoretical modeling. R.K. and T.K. wrote the manuscript with input from J.F. and J.K. **Competing interests:** The authors declare that they have no competing interests. **Data materials availability:** All data needed to evaluate the conclusions in the paper are present in the paper and/or the Supplementary Materials. Experimental data used to produce the figures can be found at https://doi.org/10.5281/zenodo.4667898.

Submitted 28 January 2021
Accepted 20 April 2021
Published 4 June 2021
10.1126/sciadv.abg8118

Citation: R. Kononchuk, J. Feinberg, J. Knee, T. Kottos, Enhanced avionic sensing based on Wigner's cusp anomalies. *Sci. Adv.* **7**, eabg8118 (2021).